

Mixing of a viscoelastic fluid in a time-periodic flow

By T. C. NIEDERKORN AND J. M. OTTINO

Department of Chemical Engineering, Robert R. McCormick School of Engineering and Applied Science, Northwestern University, Evanston, IL 60208, USA

(Received 31 August 1992 and in revised form 17 May 1993)

We present an experimental and computational investigation of mixing of a viscoelastic fluid in two-dimensional time-periodic flows generated in an eccentric cylindrical geometry. The objective of the study is to investigate the impact of fluid elasticity on the morphological structures produced by the advection of passive tracers in chaotic flows. The relevant dimensionless numbers that quantify the rheological differences with respect to the Newtonian fluid are the Deborah number (De), defined as the ratio of the fluid timescale to the flow timescale, and the Weissenberg number (We), defined as the product of the fluid timescale and the mean shear rate. The effects of elasticity are investigated in the limit of slow flows, $De \approx 0$ and $We < 0.1$. The experimental window of We is limited to Newtonian behaviour on the low end and the transition to three-dimensional flow on the high end; experiments show that this window is small, $0.02 < We < 0.1$. Typical values of the Reynolds number and the Strouhal number are $O(0.001)$ and $O(0.1)$, respectively.

Results from experiments with a constant-viscosity elastic fluid and computations using the upper-convected Maxwell constitutive equation are presented. Even though the streamlines for the elastic flow are nearly indistinguishable from the Newtonian flow, small deviations in the velocity field produce large effects on chaotically advected patterns. Elasticity affects both the asymptotic coverage of a dyed passive tracer and the rate at which the tracer is stretched. In all cases the tracer undergoes exponential stretching, but on a longer timescale as the elasticity increases. According to flow conditions, elasticity might increase or decrease the degree of regularity; however, island symmetry does not seem to be affected. Similar phenomena are observed in both the experiments and computations; therefore, an analysis of the chaotic dynamics of the periodic flow using numerical techniques is possible.

1. Introduction

Mixing of viscoelastic fluids is important in a variety of industrial applications such as processing of polymers solutions and melts (Elemans 1989; Middleman 1977; Rauwendaal 1991; Tadmor & Gogos 1979). However, in spite of recent advances in understanding mixing processes, especially those aspects connected with chaotic mixing, there is a dearth of systematic studies of mixing of viscoelastic fluids in well-characterized flows. Part of the problem is undoubtedly due to the difficulties associated with computing the velocity field of viscoelastic fluids in relatively simple configurations (Crochet, Davies & Walters 1984; Keunings 1989). Nevertheless, even though this is a rather difficult point and a general area of much ongoing research (Pilitsis & Beris 1989; Burdette *et al.* 1989; Debbaut, Marchal & Crochet 1988), an analysis of the chaotic mixing of viscoelastic fluids seems within reach, particularly in

the case of slow, two-dimensional, time-periodic flows. Such is the objective of this paper.

It is now well known that if a two-dimensional velocity field is steady the velocity field is integrable and the system cannot be chaotic (Aref 1984). On the other hand, if the velocity field is time-periodic, the phase space of the system has one more dimension, and there is a good chance that the system will be chaotic. Indeed such systems appear to be common in practice and a few have been studied experimentally and computationally (Aref 1984; Chien, Rising & Ottino 1986; Chaiken *et al.* 1986; Leong & Ottino 1989; Swanson & Ottino 1990). Almost without exception experimental studies have focused on the stirring of passive dyes in Newtonian fluids operating under time-periodic, two-dimensional Stokes flow. In fact, the only published work we are aware of that focuses on the advection of passive tracers in an elastic fluid is a short experimental study by Leong & Ottino (1990).

The typical dye structure generated in chaotically advected flows consists of islands, where the fluid stretches and contracts in a periodic manner resulting in a net twist with little stretching, dispersed within a sea of chaos where the tracer is stretched exponentially and folded in an iterative manner. Typically, the most visible islands are those associated with low-order periodic elliptic points (for a review of these issues, see Ottino 1989). Stokes flow produces a number of simplifications in the island structure, symmetry and rate independence being the most important. The islands are arranged in a symmetric pattern since the underlying streamlines are symmetric (as a result of symmetric flow domains) which results in symmetric placement of the elliptic periodic points in the flow. Moreover, the island structure is independent of the actual speed of the experiment. For example, in the case of flow between two eccentric cylinders, the dye structures are independent of the rate of rotation of the cylinders (or in the case of both cylinders rotating simultaneously, only dependent on the ratio of angular speeds). Consequently, as long as the Reynolds and Strouhal numbers are small, the mixing morphology is characterized solely by the displacement of the boundary during a period (Swanson & Ottino 1990). This independence of rate is lost in the case of elastic fluids because of the presence of an additional timescale associated with the relaxation of the fluid to its stress environment. The speed of the boundaries, or equivalently, the shear rate, now plays an important role in the mixing effectiveness.

The relative importance of rheological differences from Newtonian behaviour is quantified by the Weissenberg (We) and Deborah (De) numbers (Bird, Armstrong & Hassager 1987),

$$We = \lambda_1 |\dot{\gamma}| \quad (1)$$

and

$$De = \lambda_1 / T_{flow}, \quad (2)$$

where λ_1 is the (longest) fluid relaxation time, T_{flow} is the characteristic timescale of the flow (a timescale during which a typical fluid element experiences significant kinematical changes), and $|\dot{\gamma}|$ is the mean shear rate. For steady flows these two numbers are, in general, equivalent since both $|\dot{\gamma}|$ and T_{flow} are equal to the ratio of a characteristic length L to a characteristic velocity V . For time-periodic flows with period T , characterized by a Strouhal number,

$$Sr = L/TV, \quad (3)$$

the period T can be taken as T_{flow} , and the Deborah number can be considered as the product of Sr and We . The material behaves as a Newtonian fluid in the limit of $We = 0$ and as a purely elastic solid as De approaches infinity.

The objective of this paper is to investigate systematically the impact of fluid elasticity on the morphological structures produced by the advection of passive tracers in time-periodic flows. The goal is to extend previous studies involving Newtonian fluids and to provide a rationalization of the effects of elasticity on chaotic advection. Both an experimental study using a simple constant-viscosity fluid (Boger 1977) and a computational study using the upper-convected Maxwell constitutive equation are presented. Both studies are performed for a two-dimensional flow between eccentric cylinders. There are several reasons for these choices. The use of Boger fluids allows the separation of shear-thinning effects from those of elasticity and facilitates comparison between experimental and computational results. The Maxwell constitutive model can be simulated using a relatively simple finite-difference algorithm which works well under conditions of low We . The eccentric cylindrical geometry allows comparisons with a well-characterized Newtonian system (Swanson & Ottino 1990) with an analytical solution (Ballal & Rivlin 1976) and avoids numerical problems associated with the presence of corner singularities as in, for example, cavity flows. Moreover, the cylinders can be operated in either counter-rotating or corotating modes, producing two fundamentally different flows from a kinematical viewpoint. The counter-rotating case contains an elliptic and a hyperbolic stationary point while the corotational case contains neither.

Most of the previous work in computational non-Newtonian fluid dynamics has been in the area of steady flows (Keunings 1989). To our knowledge, no computational study has focused exclusively on time-periodic flows. Since it is well established that simulating viscoelastic flow is computationally expensive, it is appropriate for a first study to investigate the effects of elasticity in the limit of slow flows, $De \approx 0$, $We < 0.1$, and Reynolds number $Re < 0.1$. Consequently, as shown by the results in §4, the time-periodic elastic flow can be approximated by a piecewise-steady flow. The experiments are limited to slow flows because of a transition to three-dimensional flow for $We > 0.1$. Nevertheless, the observations made at these relatively small values of We provide noticeable manifestations of the effect of elasticity.

The paper is organized as follows. Section 2 presents the experimental aspects of the study including preparation and rheological behaviour of the viscoelastic fluids and a description of the design and operation of the eccentric cylindrical apparatus. Section 3 discusses the mathematical model and key assumptions pertaining to the computational study. Section 4 compares the results from the experiments and the computations, and the effect of elasticity is addressed. Finally, §5 discusses the role elasticity plays in counter-rotating versus corotating operation and summarizes the interpretation of the results.

2. Experimental methods

2.1. *Experimental fluids and rheological properties*

Non-Newtonian fluids typically possess elasticity and a shear-rate-dependent viscosity. In order to uncouple these effects, we use a constant-viscosity elastic fluid. These fluids are typically made by the addition of a small quantity of a high-molecular-weight polymer to a viscous Newtonian solvent (Boger 1977). The shear viscosity of the solvent dwarfs any polymer contribution, resulting in a constant viscosity. Additionally, the large solvent viscosity promotes the elasticity of the fluid as the polymer molecules try to relax against a large viscous resistance. Although the rheological details are significantly different, the elasticity of Boger fluids can approach that of a typical polymer melt.

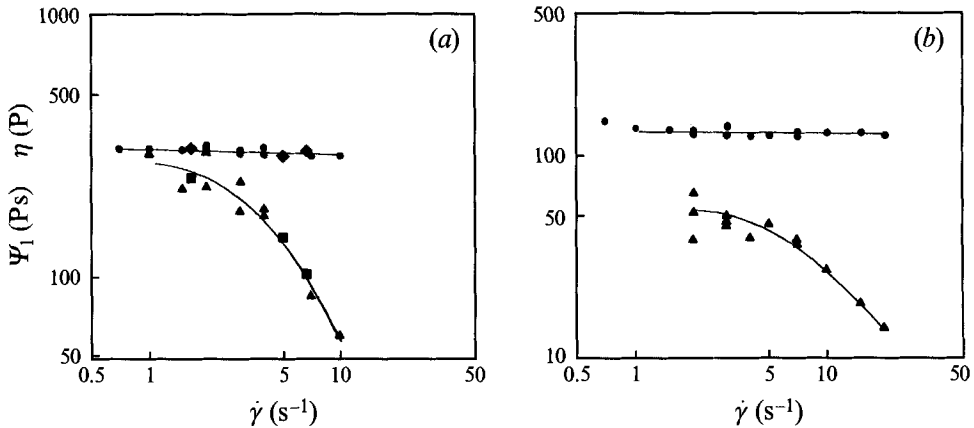


FIGURE 1. First normal stress coefficient, Ψ_1 , and shear viscosity, η , versus shear rate, $\dot{\gamma}$. (a) Fluid PAA-1; (b) fluid PAA-3: \bullet , η at temperature $T = 27^\circ\text{C}$; \blacklozenge , η at $T = 21^\circ\text{C}$ shifted; \blacktriangle , Ψ_1 at $T = 27^\circ\text{C}$; \blacksquare , Ψ_1 at $T = 21^\circ\text{C}$ shifted. The shift factor for both η and Ψ_1 for $T = 27^\circ\text{C}$ to $T = 21^\circ\text{C}$ is 1.6.

The fluid system in this study is a polyacrylamide (Scientific Polymer Products, $5\text{--}6 \times 10^6$ MW) solute in a corn syrup (American Sweeteners, 4362)/water solvent. The polymer concentration is held constant at 100 p.p.m. throughout the study. The polymer is first dissolved in water at a 1% weight concentration. The polyacrylamide/water solution is then introduced into the corn syrup/water solvent at a 1% weight concentration to produce a 100 p.p.m. polymer concentration. Before the addition of the polymer solution, the corn syrup is heated to $40\text{--}50^\circ\text{C}$ to reduce its viscosity. The solution is stirred for 8–10 h at 40°C to allow for complete polymer dispersal. The solution is then transferred into glass cylinders which are placed in the mixing apparatus. Before the fluid is loaded into the cylinder, a thin layer (5 mm) of a high-density low-viscosity fluid (Aldrich, Fomblin[®] Y-L VAC 06/6 vacuum pump oil, 31,792-6) is placed on the bottom to minimize any flow effects from the bottom surface of the cylinder. The viscoelastic fluid is then carefully poured on top of this layer to a depth of about 8 cm, followed by a 3 mm layer of mineral oil (Aldrich, 33,077-9) to prevent the formation of a skin caused by water evaporation. During the blending of the polymer solution and corn syrup, air entrainment unavoidably leads to the presence of bubbles which affects the flow and the quality of the photography; consequently, the solutions must sit for 6–8 days to allow the bubbles to rise out of the solution. Within this time frame, only air bubbles whose radius is $O(10^{-4})$ cm remain in the solution.

The relaxation time of the fluid is adjusted by varying the solvent viscosity through manipulation of the water content. Two different water concentrations are used, 1% (PAA-1) and 3% (PAA-3) by weight, to allow for a change in We without a concomitant change in the rotation speed of the cylinders. Consequently, Re and We can be adjusted independently. The use of two fluids also provides greater flexibility in setting the boundary velocity. Because the amount of light available for the photography is limited, the motion needs to be sufficiently slow so that the shutter speed needed for proper exposure is able to stop the flow.

The rheological characterization of the experimental fluids was completed by Dr R. G. Larson at AT & T Bell Laboratories. Plots of the shear viscosity, η , and first normal stress difference coefficient, Ψ_1 , are presented in figure 1. The constant-viscosity curve indicates that the fluid is indeed a Boger fluid which suggests using an Oldroyd-

Fluid	λ_1 (s)	η (P)	ρ (g/cm ³)
PAA-1 ⁽¹⁾	0.40 ± 0.10	400 ± 20	1.42 ⁽³⁾
PAA-3 ⁽¹⁾	0.20 ± 0.06	200 ± 10	1.42 ⁽³⁾
Mineral Oil ⁽²⁾	—	0.35	0.88
Y.L. VAC 06/6 ⁽²⁾	—	1.20	1.88

TABLE 1. Fluid properties. (1) $T = 27^\circ\text{C}$; (2) $T = 23^\circ\text{C}$; (3) density of pure corn syrup

type rheological model (Bird *et al.* 1987); the error in η is estimated to be $\pm 5\%$. Even though Ψ_1 exhibits shear thinning at higher shear rates, it is essentially constant in the range of shear rates of the experiments ($\dot{\gamma} < 0.4 \text{ s}^{-1}$). There is a fair amount of scattering of the Ψ_1 data because of the small signal at the low-shear-rate plateau. The error is estimated to be $\pm 25\%$ in figure 1(a) for PAA-1 and $\pm 20\%$ in figure 1(b) for PAA-3. The relaxation time is obtained from the zero-shear-limit of Ψ_1 (Bird *et al.* 1987),

$$\lambda_1 = \Psi_{1,0}/2\eta. \tag{4}$$

Since the experiment is sensitive to temperature, measurements were made at two temperatures for PAA-1 and a shift factor is used to interpolate a relaxation time or viscosity for an intermediate temperature. The fluid properties are summarized in table 1.

2.2. Apparatus and operation

The flow apparatus consists of two cylinders whose axes are parallel but not coincident. The apparatus is a new design based on that used in Swanson & Ottino (1990) and Tjahjadi & Ottino (1991). The geometry is specified by a dimensionless gap and a dimensionless eccentricity which are defined respectively as

$$\mu = \frac{r_{out}}{r_{in}} - 1 \tag{5}$$

and

$$\epsilon = \frac{e}{r_{out} - r_{in}}, \tag{6}$$

where e is the eccentricity, the distance between the cylinder centres, and r_{out} and r_{in} are the radii of the cylinders. The geometry and apparatus are illustrated in figure 2. Removable glass cylinders make preparation and loading of the viscoelastic fluid a simple task: the glass cylinders are mounted on the stand after the fluid is loaded into the outer cylinder. Although the geometry is kept constant in this study, this design also allows for a wide range of variations.

The inner and outer cylinders are made of Pyrex and are 2.2 cm OD and 6.6 cm ID, and the geometrical parameters for this system are $\mu = 2.0$ and $\epsilon = 0.45$. There are two major components to the apparatus: a drive section and a control section. The drive section consists of two motors, gearing and adapters to hold each cylinder. The control section consists of a 286 PC computer with associated input and output signal generators. The computer sends an input digital signal to a D/A converter which supplies a voltage to the motor controllers. Tachometers on each motor provide a feedback output signal to the computer via an A/D converter. The angular rotation can be controlled within $\pm 2\%$.

We and Re for flow in this geometry are defined as

$$We = \lambda_1 V / r_{in} \mu \tag{7}$$

and

$$Re = \rho V r_{in} \mu / \eta, \tag{8}$$

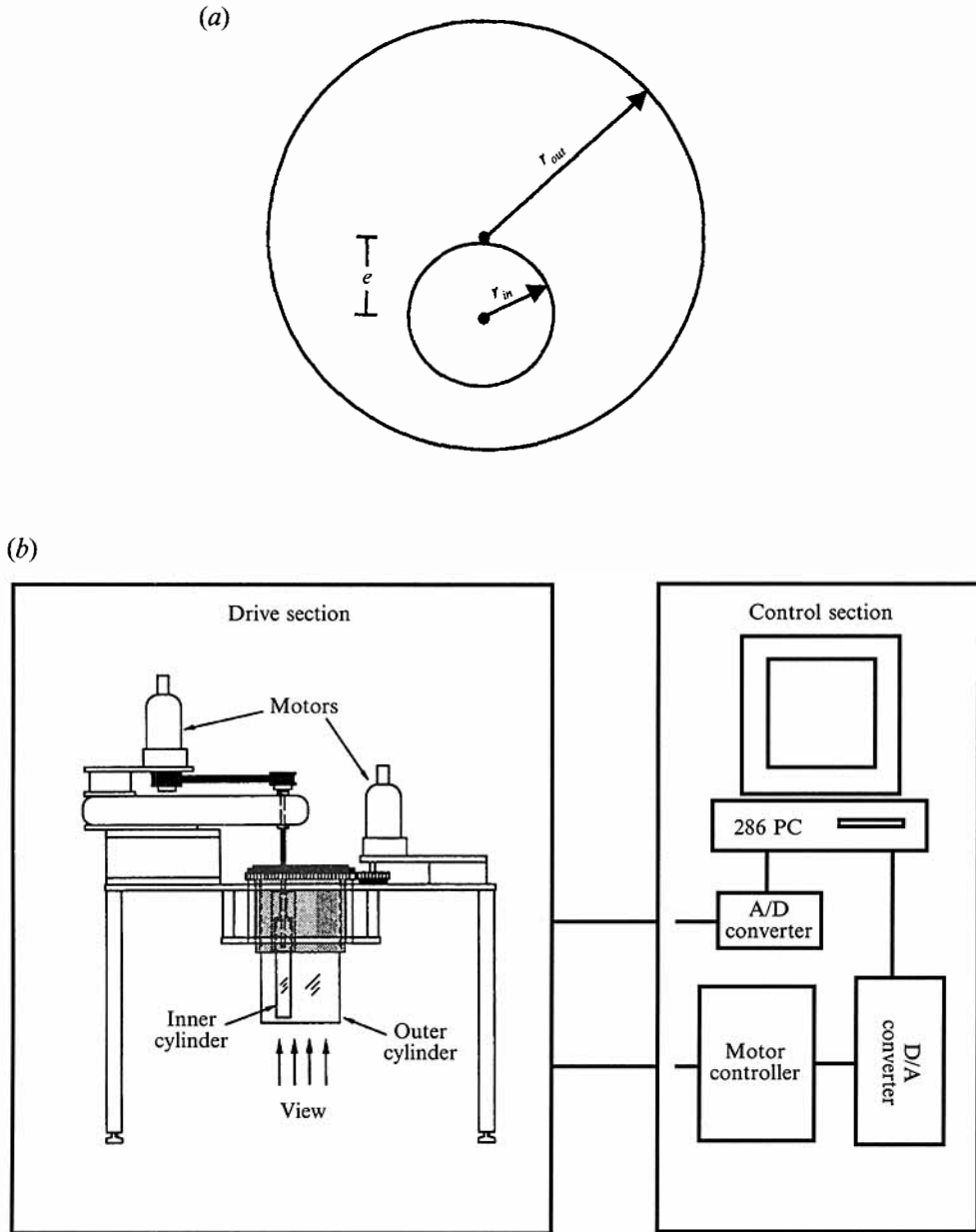


FIGURE 2. (a) Eccentric cylindrical geometry; (b) experimental apparatus.

where ρ is the density and V is the linear velocity of either cylinder. The shear-rate range of the apparatus is from 0.06 to 0.37 s^{-1} which corresponds to an experimental range of We from 0.02 to 0.24 and Re from 0.005 to 0.06 for this particular fluid system at 21°C . Given the uncertainties in the values of λ_1 and V , the experimental error in the value of We is estimated to be $\pm 32\%$ for fluid PAA-3 and $\pm 27\%$ for fluid PAA-1.

Flow visualization is accomplished by the advection of a neutrally buoyant, passive

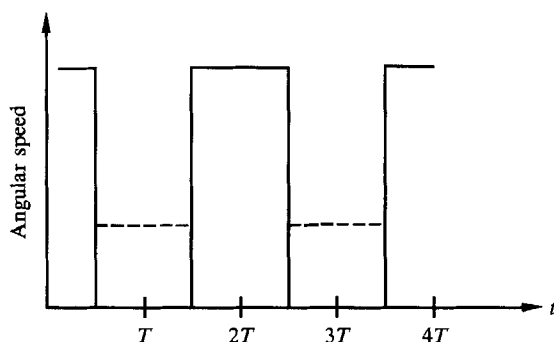


FIGURE 3. Symmetric square wave form; —, inner cylinder; ----, outer cylinder.

fluorescent tracer illuminated by long-wave UV lights (UV-A). It should be pointed out that the rheology of the tracer plays almost no role; in fact, experiments conducted with viscoelastic tracers and Newtonian tracers give nearly identical results. The experiments are recorded using a 35 mm camera, 105 mm lens with an orange filter, and 400 ASA colour slide film. Two different dyes, Cole Parmer yellow/green (295-17) or red (295-15) dye, produce satisfactory results, but the photography is more difficult than in previous experiments with glycerin (Swanson & Ottino 1990) since corn syrup radiates the absorbed UV light at a greater intensity and longer wavelength. Typical shutter speeds are $\frac{1}{4}$ or $\frac{1}{8}$ s which are sufficiently fast to stop the flow. The photographs are taken through the bottom of the outer cylinder.

Chaotic advection is accomplished by a time-periodic forcing of the boundaries. In order to keep the investigation reasonably focused, we consider only the symmetric square-wave form shown in figure 3 with the cylinders operating either in corotating or counter-rotating modes. The respective angular velocities are Ω_{in} and Ω_{out} , and the ratio of the angular velocities, Ω_{in}/Ω_{out} , is denoted as Ω . The magnitude of Ω is set equal to the ratio of the radii so that the linear speed is the same on both cylinders. Experiments are characterized by the angular displacement of the outer cylinder in a period:

$$\theta = \int_0^T \Omega_{out}(t) dt \tag{9}$$

where T is the period length.

A typical experiment is set up by injecting a tracer as a small blob of dye about 4 cm below the surface of the fluid using a thick needle syringe. Since the inner cylinder rotates first, the tracer is placed near the inner cylinder so that it is stretched immediately. The cylinders are then rotated in a discontinuous manner, as indicated by the wave form in figure 3, for a number of periods, N . Photographs are taken at the end of each period when the symmetry of the dye structures, indicative of symmetric velocity fields, is most apparent. Typical values of θ are $\frac{3}{2}\pi$, 2π , and 4π . Experiments for different θ -values are compared at identical values of the cumulative rotation of the outer cylinder. The asymptotic dye structure in most of the flows is developed after 24π radians of rotation of the outer cylinder which corresponds to 16, 12, and 6 periods, respectively, for these values of θ .

3. Computational methods

3.1. Mathematical model

Viscoelastic flow is modelled in terms of the continuity equation, momentum equation, and a suitable (either rate or integral) constitutive equation (Bird *et al.* 1987). The development of algorithms to solve viscoelastic flows has been hampered by what is known as the *high-We problem*, that is, algorithms fail at relatively low We , $O(1)$ (Crochet *et al.* 1984; Keunings 1989; Joseph 1990). Consequently, a great deal of analytical work has been done on examining the differential equations describing the flow, and recent developments indicate significant progress has been made in handling higher We flows (Pilitsis & Beris 1989; Burdette *et al.* 1989; Debbaut *et al.* 1988). It has been shown as well that viscoelastic constitutive equations contain some hyperbolic character and are capable of changing type and losing evolution (Rutkevich 1969; Joseph, Renardy & Saut 1985; Dupret & Marchal 1986). It is therefore apparent that computations can be aided by exploiting the hyperbolic character of the system of governing equations. This can be achieved by a suitable handling of the mass-conservation constraint. The algorithm developed by Phelan, Malone & Winter (1989) employs a compressible form of the continuity equation to form a purely hyperbolic set of equations. Consequently, a robust algorithm originally developed for hyperbolic equations in compressible gas flows can be used to simulate the flow of a Maxwell fluid. Since the algorithm is based on finite differences, it is relatively easy to implement.

The compressible form of the continuity equation is derived as follows for isothermal flow. The convective derivative of density is proportional to the convective derivative of pressure:

$$\frac{D\rho}{Dt} = \frac{\rho}{\kappa} \frac{Dp}{Dt}, \quad (10)$$

where κ is the inverse of the isothermal compressibility. Substituting (10) into the continuity equation yields the isothermal compressible continuity equation:

$$\frac{Dp}{Dt} + \kappa(\nabla \cdot \mathbf{v}) = 0. \quad (11)$$

The isothermal compressibility has been measured for polymer solutions and a physically realistic value for κ (10^4 atm) is used in the computation (Phelan 1989). Since the flow is nearly incompressible (κ large), compressibility effects in both the momentum and constitutive equation are neglected. The derivation of (11) is not based on a Taylor series expansion as presented in Phelan *et al.* (1989). Consequently, (11) is valid for any isothermal flow, and there is no restriction about a Taylor series expansion point.

The extra-stress tensor \mathbf{S} is related to the deformation of the fluid by the upper-convected Maxwell model,

$$\lambda_1 \left[\frac{D\mathbf{S}}{Dt} - (\nabla \mathbf{v})^T \cdot \mathbf{S} - \mathbf{S} \cdot \nabla \mathbf{v} \right] + \mathbf{S} - \eta[\nabla \mathbf{v} + (\nabla \mathbf{v})^T] = \mathbf{0}. \quad (12)$$

This relation is the simplest rate equation that can describe a fluid with memory. The equation contains two parameters, the shear viscosity, η , and the relaxation time, λ_1 . The model predicts a constant shear viscosity which is appropriate for the experimental fluid. In addition, the Maxwell model cannot change type in inertialess flows. A

description of the algorithm used to simulate the flow of the Maxwell fluid is presented in §3.3.

3.2. Dimensional analysis

The complete equation set to describe viscoelastic flow includes the momentum equation in addition to (11) and (12). If the characteristic velocity, length, and stress in this model are defined as $r_{in} \Omega_{in}$ ($= r_{out} \Omega_{out}$), $r_{in} \mu$, and $\eta \Omega_{in} / \mu$, respectively, the complete set of governing equations in dimensionless form is given by

$$Sr \frac{\partial p}{\partial t} + v \cdot \nabla p + \kappa (\nabla \cdot v) = 0, \quad (13)$$

$$Re \left(Sr \frac{\partial v}{\partial t} + v \cdot \nabla v \right) + \nabla p - \nabla \cdot \mathbf{S} = 0, \quad (14)$$

and $We \left[Sr \frac{\partial \mathbf{S}}{\partial t} + v \cdot \nabla \mathbf{S} - (\nabla v)^T \cdot \mathbf{S} - \mathbf{S} \cdot \nabla v \right] + \mathbf{S} - [\nabla v + (\nabla v)^T] = 0, \quad (15)$

where $Sr = \mu / T_{flow} \Omega_{in}, \quad (16)$

$$Re = \rho r_{in}^2 \mu \Omega_{in} / \eta, \quad (17)$$

and $We = \lambda_1 \Omega_{in} / \mu. \quad (18)$

According to this choice, the stress is scaled by $\eta V/L$. However, the stress can also be scaled by η/λ_1 . The momentum and constitutive equations are scaled identically for the two different choices when $We = 1$. We choose this scaling of the stress since $We < 0.1$ for all flows presented in this paper. A discussion on the scaling of viscoelastic flow equations can be found in Joseph (1990).

For time-periodic flow, the appropriate choice for the flow timescale is the period length, T . If the period is sufficiently long ($Sr \ll 1$), the transient fields can be neglected, and the time-periodic flow can be simulated as a sequence of steady flows. This is a crucial assumption as the time required to simulate the flow is reduced by a factor equal to the number of periods: typical CPU times are reduced by at least an order of magnitude.

Since Re , We , and Sr are small, the physics can be considered a perturbation of Stokes flow. The Weissenberg number is usually interpreted as the ratio of elastic forces to viscous forces; similarly, the Reynolds number characterizes the ratio of inertial forces to viscous forces; hence, the relative corrections to the Stokes solution due to elasticity and inertia is characterized by the Elasticity number (Astarita & Marrucci 1974),

$$El = We/Re = \lambda_1 \eta / \rho r_{in}^2 \mu^2. \quad (19)$$

Note that El is a function of the physical constants of the fluid and the geometry and independent of the characteristic velocity. If $El \gg 1$, the correction to Stokes flow will be dominated by the effects of elasticity.

3.3. Algorithm

The entire set of the compressible continuity equation, the Maxwell constitutive equation, and the momentum equation ((13)–(15)) form a purely hyperbolic system. The steady velocity, stress, and pressure fields are computed by integrating the coupled equation set to steady state using a method-of-lines approach with the split coefficient matrix (SCM) algorithm originally developed for compressible gas flows (Anderson,

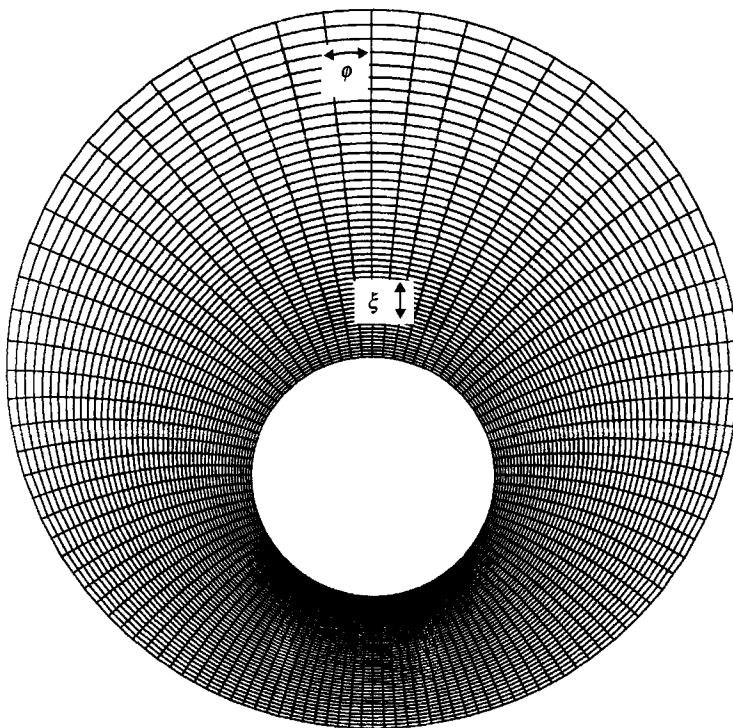


FIGURE 4. 49×96 computational finite-difference grid in bipolar coordinate system.

Tannehill & Pletcher 1984). The algorithm manages the hyperbolic character of the equation set by splitting the coefficient matrix along the directions of the characteristics of the system. The spatial derivatives are approximated with either forward or backward finite differences depending on the eigendirections. We have improved the algorithm (SCM-star) to increase its speed: instead of splitting the matrices, a combination of the original coefficient matrix and one based on the absolute values of the eigenvalues performs the same task. Details of this improvement are provided in the Appendix.

A bipolar coordinate system (ξ, ϕ) is used to discretize the spatial domain in the eccentric annulus. The transformation is defined as

$$x = \frac{a \sinh \xi}{\cosh \xi + \cos \phi} \quad (20)$$

and

$$y = \frac{a \sin \phi}{\cosh \xi + \cos \phi}, \quad (21)$$

where a is a geometrical parameter based on the eccentricity and the radii,

$$a = r_{in} \frac{(1 - \epsilon^2)^{\frac{1}{2}}}{\epsilon} \left[1 + \mu + \mu^2 \left(\frac{1 - \epsilon^2}{4} \right)^{\frac{1}{2}} \right]. \quad (22)$$

In order to capture the chaotic dynamics with an acceptable amount of error, a relatively fine grid is used consisting of 49 radial nodes and 96 azimuthal nodes. The grid is presented in figure 4. This choice was based on computations done by Swanson (1991) on chaotic advection using a *discretized* form of the analytical solution for

Stokes flow and comparing the results to the original exact solution. Using a first-order interpolation method, the results in Swanson (1991) indicate that about 5000 nodes are necessary to accurately reproduce the results of the analytical solution.

Another consideration for the grid size is the accuracy of the solution of the partial differential equation set (13)–(15). To confirm that the results are a manifestation of the physical phenomena being modelled and not a numerical artifact, solutions are computed on three different sizes: 37×72 , 49×96 , and 97×192 . The solution of the system of partial differential equations converges with grid spacing, indicating that the results are not a numerical artifact. The solutions for the two grids with the smallest spacing (49×96 and 97×192) nearly overlap one another. This indicates that the 49×96 grid is of sufficient accuracy for the solution of the system of partial differential equations.

3.4. Methods of analysis

The experiment can be simulated by discretizing the boundary of a tracer with a set of points and integrating their trajectories. However, because of the exponential rate of stretching present in these flows, it would take a prohibitive number of points to track the material surface of the tracer (Franjione & Ottino 1987). There are other possibilities though. The dye pattern has a considerable degree of self-similarity, and folds present in early periods remain throughout the experiment as details are added on a finer and finer scale (Muzzio, Swanson & Ottino 1991). An accurate picture of the structure of the folds after N periods can be achieved by plotting all of the positions corresponding to the previous periods. This type of simulation provides a much more efficient use of CPU time and a faithful representation of the experimentally observed dye structure. The initial shape of the tracer is represented as a ‘square’ in the bipolar frame and consists of 10201 points. The initial location and size are similar to those in the experiments. A second-order Runge–Kutta (midpoint) method is used to integrate the particle trajectories, and a bilinear interpolation is used to calculate the velocity between the nodal points.

Chaotic flow provides a stringent test of numerically computed velocity fields: small errors in the velocity field are magnified by the chaotic dynamics. The numerical code is validated in two steps for a chaotic flow. The experimental photograph in figure 8(a) is used for comparison with the computed solutions. First, a simulation is done using the discretized analytical Stokes solution on the 49×96 grid with the midpoint integration method and bilinear interpolation, and the result is presented in figure 8(b). This comparison indicates that the integration, interpolation, and grid are of sufficient accuracy. Second, a computation is done using the viscoelastic algorithm in the Stokes limit, We and $Re \rightarrow 0$. The algorithm contains singularities at either $We = 0$ or $Re = 0$ since the reciprocal of these numbers appears on the right-hand side when (13)–(15) are integrated. Numerically, the Stokes limit is reasonably approximated by $Re = We = 10^{-3}$, and the result in figure 5 demonstrates sufficient agreement with the analytical solution and the experimental photograph to validate the viscoelastic algorithm.

The simulated tracer advection computation produces the same qualitative result as the experiment. The effects of elasticity can be quantified by computing the amount of stretching for various degrees of elasticity. In order to calculate the lineal stretching rate, the deformation tensor \mathbf{F} must be computed for all material points in the flow. This requires solving the evolution equation for \mathbf{F} ,

$$\frac{d\mathbf{F}}{dt} = (\nabla\mathbf{v})^T \cdot \mathbf{F}; \quad \mathbf{F}_{t=0} = \mathbf{I}, \quad (23)$$



FIGURE 5. Viscoelastic simulation in the Stokes limit for $\theta = \frac{3}{2}\pi$ and $\Omega < 0$; $We = 10^{-3}$ and $Re = 10^{-3}$.

as well as the evolution equation for the spatial coordinate of the material point,

$$\frac{d\mathbf{x}}{dt} = \mathbf{v}; \quad \mathbf{x}_{t=0} = \mathbf{X}. \quad (24)$$

The stretching rate λ is defined as

$$\lambda = \lim_{d\mathbf{X} \rightarrow 0} \frac{|d\mathbf{x}|}{|d\mathbf{X}|} \quad (25)$$

and

$$d\mathbf{x} = \mathbf{F} \cdot d\mathbf{X}, \quad (26)$$

where $d\mathbf{X}$ is an infinitesimally small fluid line at $t = 0$ and $d\mathbf{x}$ is the fluid line at some later time t . Since the stretching rate is exponential, the timescale T_c is defined as

$$\bar{\lambda} = \exp(t/T_c), \quad (27)$$

and $\bar{\lambda}$ is the geometric mean of the spatially distributed values of λ .

This method is time consuming but accurate for an analytical velocity field and such an approach was used by Swanson & Ottino (1990). However, to compute λ for a discretized velocity field, the method is not as accurate since the velocity gradients in (23) are computed numerically from the nodal values of the velocity. A simpler and still reasonably accurate calculation can be done by measuring the distance, d , between two 'adjacent' material points as they are separated by the flow. As with the stretching rate, we would expect the rate of separation to occur exponentially in time in the chaotic flow. We should note that, although d is comparable with the lineal stretching during the initial part of the computation, the correspondence is diminished once a tracer of

similar dimension to the initial separation distance begins to fold. An analogous time constant T_c can be extracted from this calculation:

$$\bar{d} = \exp(t/T_c), \tag{28}$$

which \bar{d} is the geometric mean of the spatially distributed values of d .

To perform the calculation, two points are placed near the centre of a nodal box along a constant value of ϕ and separated in the ξ -direction by an initial separation distance d_0 . The two points in each nodal box are advected by the flow and the distance between them is tracked. This procedure is repeated for all of the nodal boxes resulting in a spatial distribution of d . It is observed in the periodic-flow calculations that, after about 10 radians of rotation of the outer cylinder and for $d_0 = 2 \times 10^{-6}$, the connection between d and λ is lost. This corresponds to about 6 periods for $\theta = \frac{3}{2}\pi$ and 5 periods for $\theta = 2\pi$.

4. Advection of elastic fluids: comparison of experiments and computations

4.1. Steady and transient velocity fields

The experimental window of Weissenberg numbers is defined by the Newtonian limit on the low end and the transition to three-dimensional flow on the high end; this window is surprisingly small, from 0.02 to 0.1. The streamlines for Stokes flow with the inner and outer cylinders rotating are presented in figure 6. For the geometry and range of We considered in this study, the streamline pattern does not change significantly although the separation bubble shrinks slightly in both cases as We increases. It should be mentioned that for the inner cylinder rotating, a reduction of the region of separated flow has also been observed experimentally with laser Doppler velocimetry by Lawler *et al.* (1986) and computationally by Beris, Armstrong & Brown (1987) for eccentric cylinders with small μ ($O(0.1)$).

The effect of elasticity on the steady velocity fields can be quantified in terms of the root-mean-square deviation of the nodal values of the elastic flow compared to the (analytical) Newtonian flow,

$$\text{r.m.s.} = \left[\frac{1}{n} \sum_1^n (v_{\text{Newtonian}} - v_{\text{elastic}})^2 \right]^{\frac{1}{2}}, \tag{29}$$

where n is the number of nodes in the interior of the flow, and the velocities are normalized with respect to $r_{in}\Omega_{in}$. Average r.m.s. values corresponding to either the inner or outer cylinder rotating range from 2.1×10^{-3} for $We = 0.01$ to 4.2×10^{-2} for $We = 0.1$. Some of the difference can be attributed to discretization error; for example, the r.m.s. value for the Newtonian limit ($We = 10^{-3}$) velocity field used to calculate figure 5 is 1.7×10^{-3} .

Because the fluid has memory, or equivalently, because of the presence of the convected derivatives in the Maxwell constitutive equation, the velocity fields are asymmetric. However, the degree of asymmetry is proportional to We , and asymmetric effects on the streamlines are not noticeable until $We \gtrsim 1$ (Beris, Armstrong & Brown 1983). Since $We \leq 0.1$, the degree of asymmetry is small, $O(10^{-4} - 10^{-3})$, in the range of We examined in this study.

Time-periodic flow is generated by rotating either the inner or outer cylinder as described in §2. The experimental range of parameters is as follows. The values of θ considered are $\frac{3}{2}\pi$, 2π , and 4π with corresponding values of the Sr equal to 0.14, 0.11,

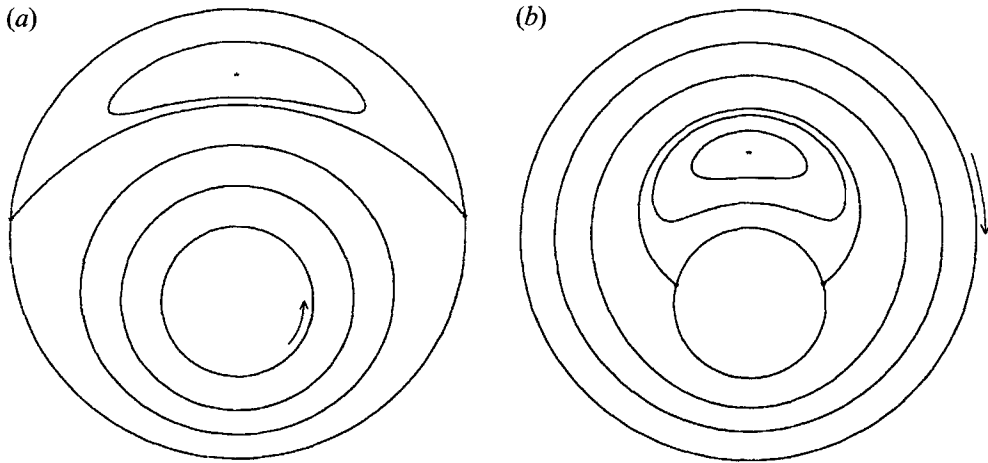


FIGURE 6. Analytical solution for Stokes flow: (a) inner cylinder rotating; (b) outer cylinder rotating.

0.05, respectively. The Re ranges from 0.002 to 0.005, and Re is set at 0.002 for the numerical computations. The value of El is between 10 to 20, indicating that the effects from elasticity are at least an order of magnitude higher than the effects of inertia.

Since the flow is considered piecewise steady in the computations, the importance of the transient velocity field in the experiment should be addressed. Two tests are performed for the $\theta = \frac{3}{2}\pi$ counter-rotating flow (this flow has a characteristic bifurcation signature which is very sensitive to small perturbations) in order to determine if the transient is significant. The first test is done with an elastic fluid with either a zero time lag between cylinder change-over or a 5 s time lag between cylinder change-over. The second test is an experiment for a Newtonian fluid with an imposed transient. An artificial transient is created by ramping the cylinder rotation speed from rest to the final set point over an interval of time equal to one-tenth of the period length. This choice is made since the maximum ratio of the dynamic relaxation time of the elastic fluid to the period length in this study is about 7%. Both of these tests indicate that the transient is insignificant as no noticeable effects on the dye pattern are observed. We conclude that the bifurcations observed in the chaotically advected dye patterns in the time-periodic flows are the result of minor changes in the steady-state velocity fields. This result is very much in line with other simulations that we have conducted involving small variations in the velocity field due to the presence of a shear-thinning viscosity.

Experiments are conducted for We between 0.05 and 0.11, and a series of computations is conducted independently for We between 0.01 and 0.1. Our intention is not necessarily to model the experimental fluid with a Maxwell constitutive equation, but rather to conduct experiments with a simple fluid and computations with a simple constitutive equation and compare the results on the impact of elasticity on chaotic advection. However, in some cases, a nearly perfect match between experimental and computed structures is possible. In making these types of comparisons, a few observations are in order. Because of the qualitative nature of the results, some flow conditions produce elaborate features which make matching the experiments and computations easy. For example, experiments with $\theta = \frac{3}{2}\pi$ and $\Omega < 0$ lead to characteristic bifurcation signatures allowing unmistakably clear matches (see figure

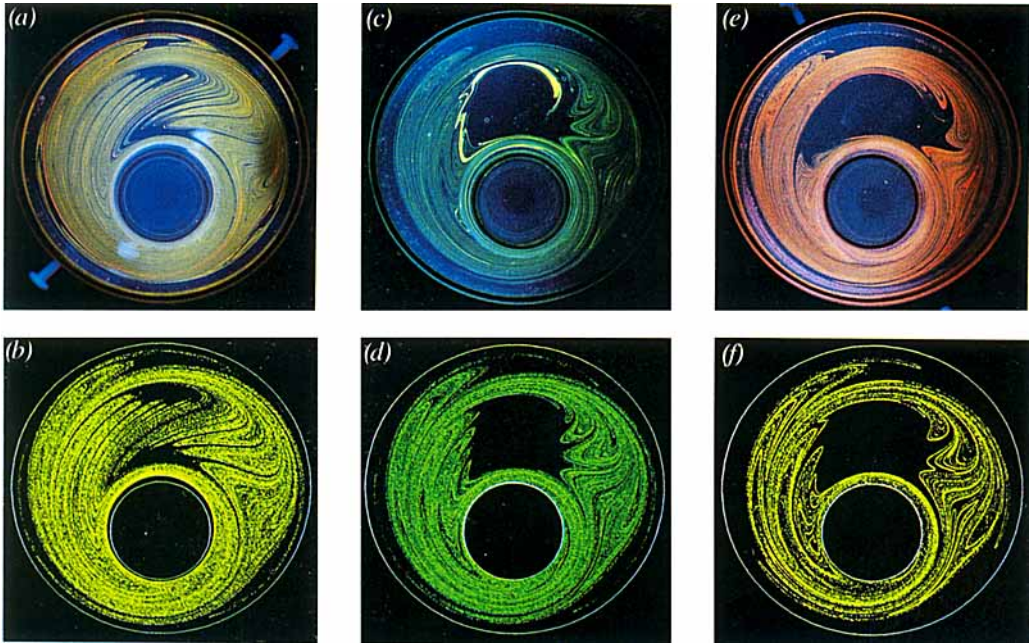


FIGURE 8. Experiments and computations on the advection of a dye blob for $\Omega < 0$ and $\theta = \frac{3}{2}\pi$. (a, b) Newtonian; (c) $We = 0.06 \pm 0.02$; (d) $We = 0.04$; (e) $We = 0.10 \pm 0.03$; (f) $We = 0.10$; (a-f) $N = 16$ periods.

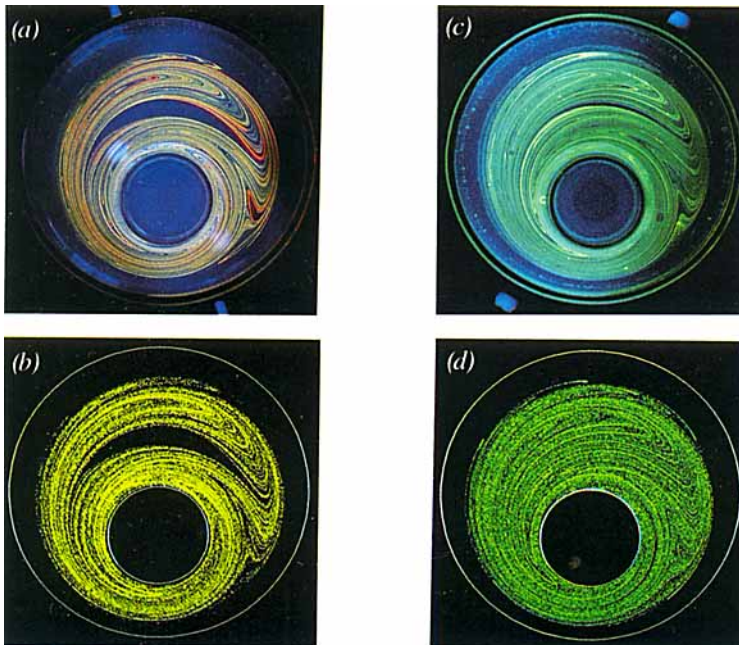


FIGURE 10. Experiments and computations on the advection of a dye blob for $\Omega < 0$ and $\theta = 2\pi$. (a, b) Newtonian; (c) $We = 0.06 \pm 0.02$; (d) $We = 0.04$; (a-d) $N = 12$ periods.

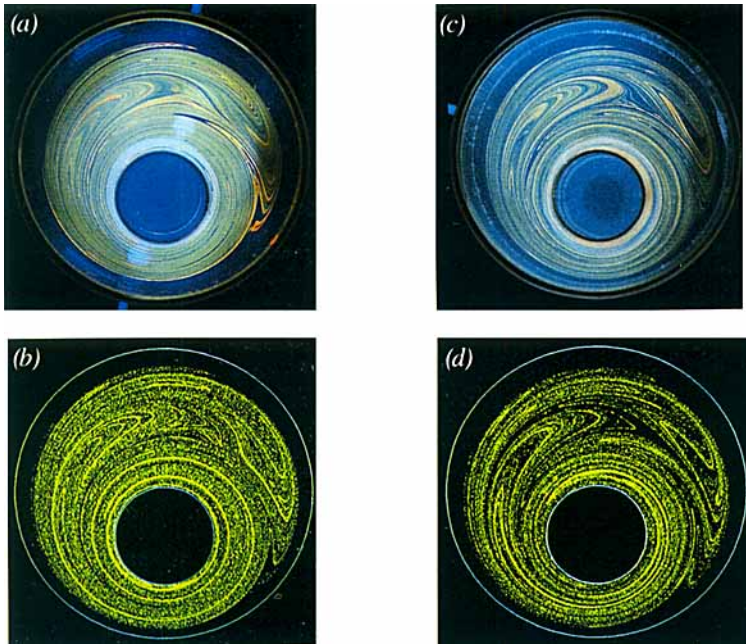


FIGURE 11. Experiments and computations on the advection of a dye blob for $\Omega < 0$ and $\theta = 2\pi$. (a, b) Newtonian; (c) $We = 0.07 \pm 0.02$; (d) $We = 0.04$; (a-d) $N = 6$ periods.

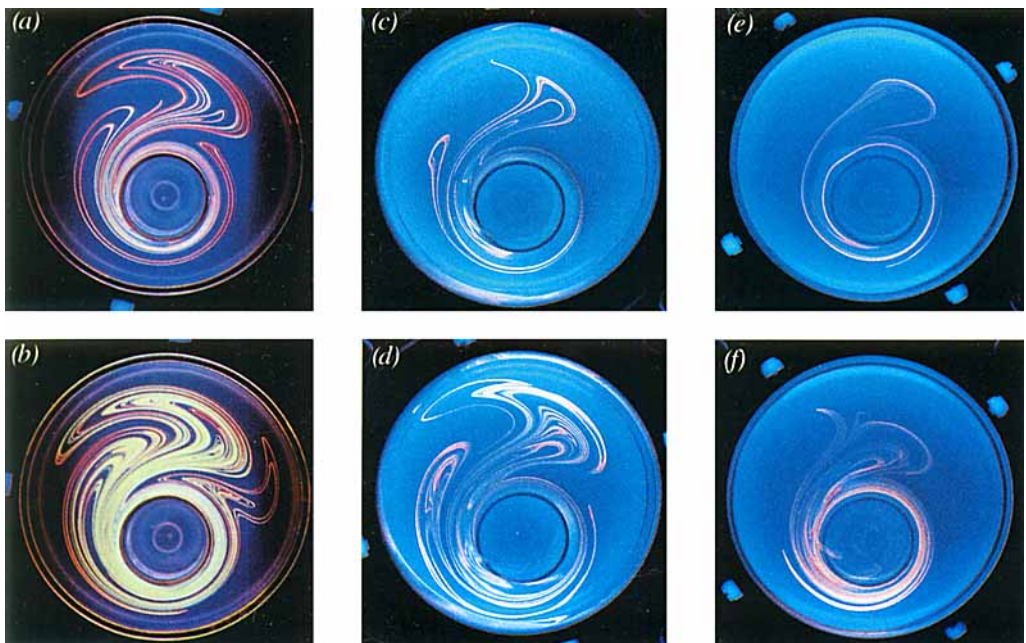


FIGURE 15. Experiments on the advection of a dye blob for $\Omega > 0$ and $\theta = \frac{3}{2}\pi$. (a, b) Newtonian; (c, d) $We = 0.05 \pm 0.02$; (e, f) $We = 0.11 \pm 0.03$; (a, c, e) $N = 3$ periods; (b, d, f) $N = 5$ periods.

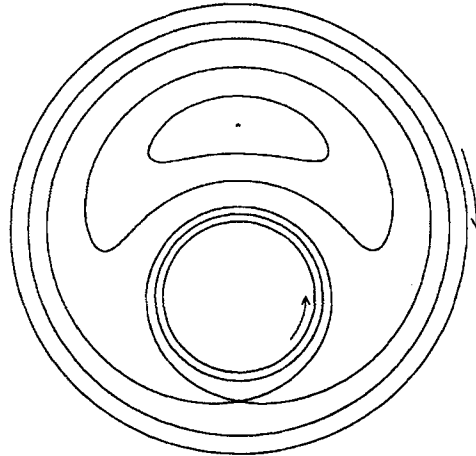


FIGURE 7. Analytical solution for Stokes flow with counter-rotating cylinders.

8). However, other flow conditions, particularly far away from island bifurcations (for example $\theta = 4\pi$), are relatively featureless and matches over a wider range in We (0.02–0.1) are possible. Even though the agreement between the experimental and computed We is not perfect, the numbers are comparable within experimental error, and the agreement is more than what can reasonably be expected from such a simple constitutive model. In §4.4, we speculate on why the Maxwell model appears to sufficiently reproduce the qualitative results of the experimental fluid.

4.2. Counter-rotating cylinders ($\Omega < 0$)

The unperturbed, counter-rotating Stokes flow is characterized by an elliptic fixed point and a saddle point, both located on the axis of symmetry. The streamlines are shown in figure 7. Under time-periodic operation, the elliptic fixed point is replaced by an elliptic period-1 point whereas the saddle point becomes a hyperbolic periodic point. For a Newtonian fluid, this elliptic periodic point is present for all $\theta < \frac{3}{2}\pi$ (Swanson & Ottino 1990), although the region of circulation in the neighbourhood of this point progressively shrinks. At $\theta = \frac{3}{2}\pi$, the elliptic point bifurcates into a hyperbolic point and two elliptic points, as illustrated by the experimental photograph and computation in figure 8(a, b) (plate 1). This flow provides a useful reference case: the bifurcation signature presents a taxing experimental example for computational matches. What happens to this bifurcation for an elastic fluid? Figure 8(c) is a photograph of fluid PAA-3 and $We = 0.06 \pm 0.02$; there is a large island which does not communicate with the rest of the spatial domain. The bright tail in the photograph results from a part of the tracer which was initially placed in the regular region and illustrates the rather substantial difference in the amount of stretching between the chaotic and regular regions. A computation for $We = 0.04$ is shown in figure 8(d) illustrating remarkable agreement with the experiment. The structure of the folds on both sides of the island demonstrate a one-to-one correspondence between the computation and experiment. The structure of the folds in other regions of the flow are also similar, if not identical. The large tail in the island is not present in the computation because of a slight difference in the initial condition. If We is increased to 0.10, the island becomes larger, as seen in both the experiment (fluid PAA-1, $We = 0.10 \pm 0.03$) and computation, figure 8(e–f). One might conjecture that the elasticity somehow inhibits the bifurcation of the elliptic point resulting in the large island and poorer mixing. However,

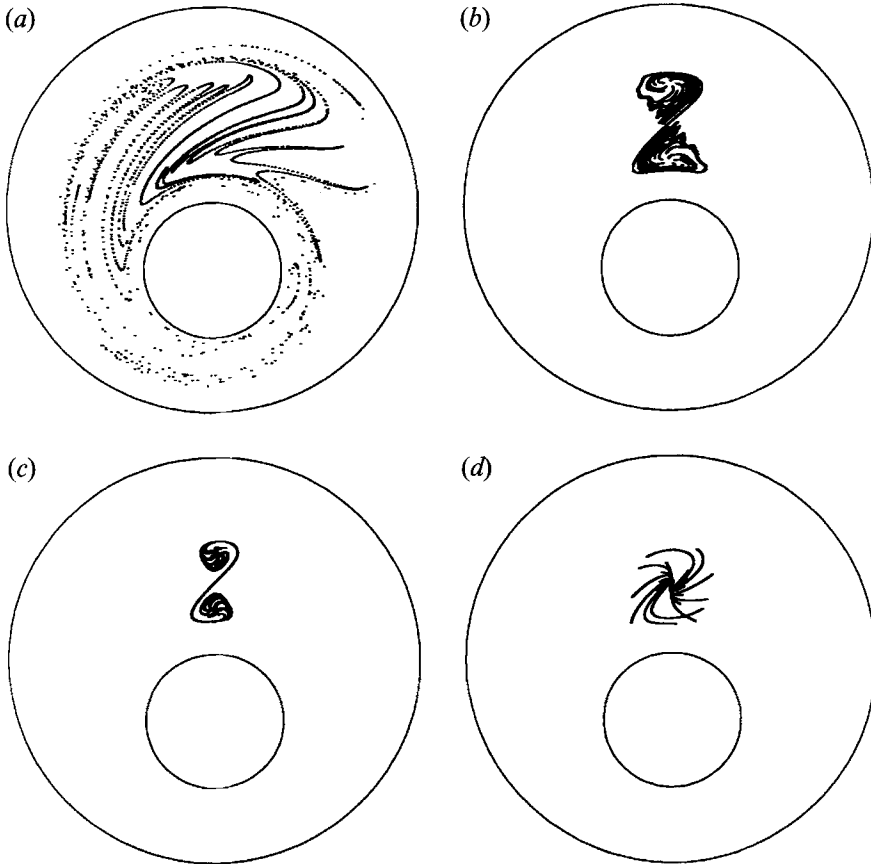


FIGURE 9. Computations of the advection of a line of points placed at the line of symmetry in the large gap for $\Omega < 0$ and $\theta = \frac{3}{2}\pi$. (a) Newtonian; (b) $We = 0.02$; (c) $We = 0.04$; (d) $We = 0.10$; (a) $N = 10$ periods; (b–d) $N = 20$ periods.

computations for $We = 0.02, 0.04$, and 0.1 in figure 9 reveal that the hyperbolic point and the pair of elliptic points are present in all of the flows. However, the region surrounding these points for $We > 0$ does not communicate with the rest of the flow because of a bounding KAM surface (Ottino 1989). Also, as the elasticity increases, the elliptic points move closer to the hyperbolic point, and it is likely that the bifurcation is inhibited at some higher We . However, verifying this conjecture would entail a considerable investment in computational resources.

Does elasticity always inhibit mixing? Figure 10 (plate 1) compares the Newtonian flow and elastic flow (fluid PAA-3, $We = 0.06 \pm 0.02$) for $\theta = 2\pi$ and illustrates that the answer is not a simple 'yes'. The crescent-shape island present in the Newtonian case has all but disappeared in the viscoelastic case. The computation likewise shows the disappearance of this island. The presence of this island is extremely sensitive to We and essentially disappears even for $We = 0.01$. The large regular region next to the outer cylinder is about the same size in both cases. For $\theta = 4\pi$, there is no difference in the asymptotic coverage of the dye between the Newtonian and elastic fluid (PAA-1, $We = 0.07 \pm 0.02$) experiments as shown in figure 11 (a, c) (plate 2). However, close examination of the photographs reveals that the average striation thickness for the Newtonian flow is much less than that of the elastic flow. This difference can be seen in the computations in figure 11 (b, d) by the degree of scattering of the points

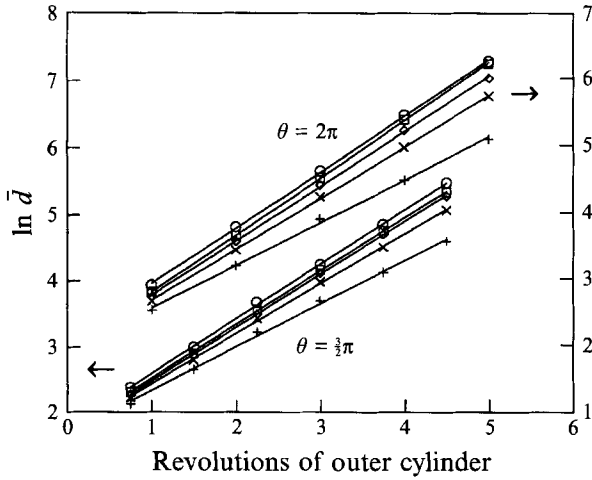


FIGURE 12. Plot of the logarithm of the geometrical mean of the distribution of the separation distances versus number of periods for $\Omega < 0$ and $\theta = \frac{3}{2}\pi$ (left axis) and $\theta = 2\pi$ (right axis): \circ , Newtonian; \square , $We = 0.01$; \diamond , $We = 0.02$; \times , $We = 0.04$; $+$, $We = 0.10$.

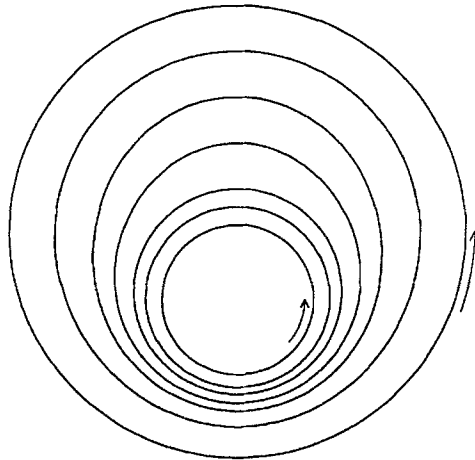


FIGURE 13. Analytical solution for Stokes flow with corotating cylinders.

We	Time constant, T_c			
	$\Omega < 0$		$\Omega > 0$	
	$\theta = \frac{3}{2}\pi$	$\theta = 2\pi$	$\theta = \frac{3}{2}\pi$	$\theta = 2\pi$
0	1.23	1.21	0.96	0.95
0.01	1.24	1.19	1.18	1.26
0.02	1.26	1.23	1.27	1.36
0.04	1.34	1.31	1.44	1.55
0.10	1.55	1.57	1.81	1.91

TABLE 2. Time constants for the exponential growth of the geometric mean of the separation distances

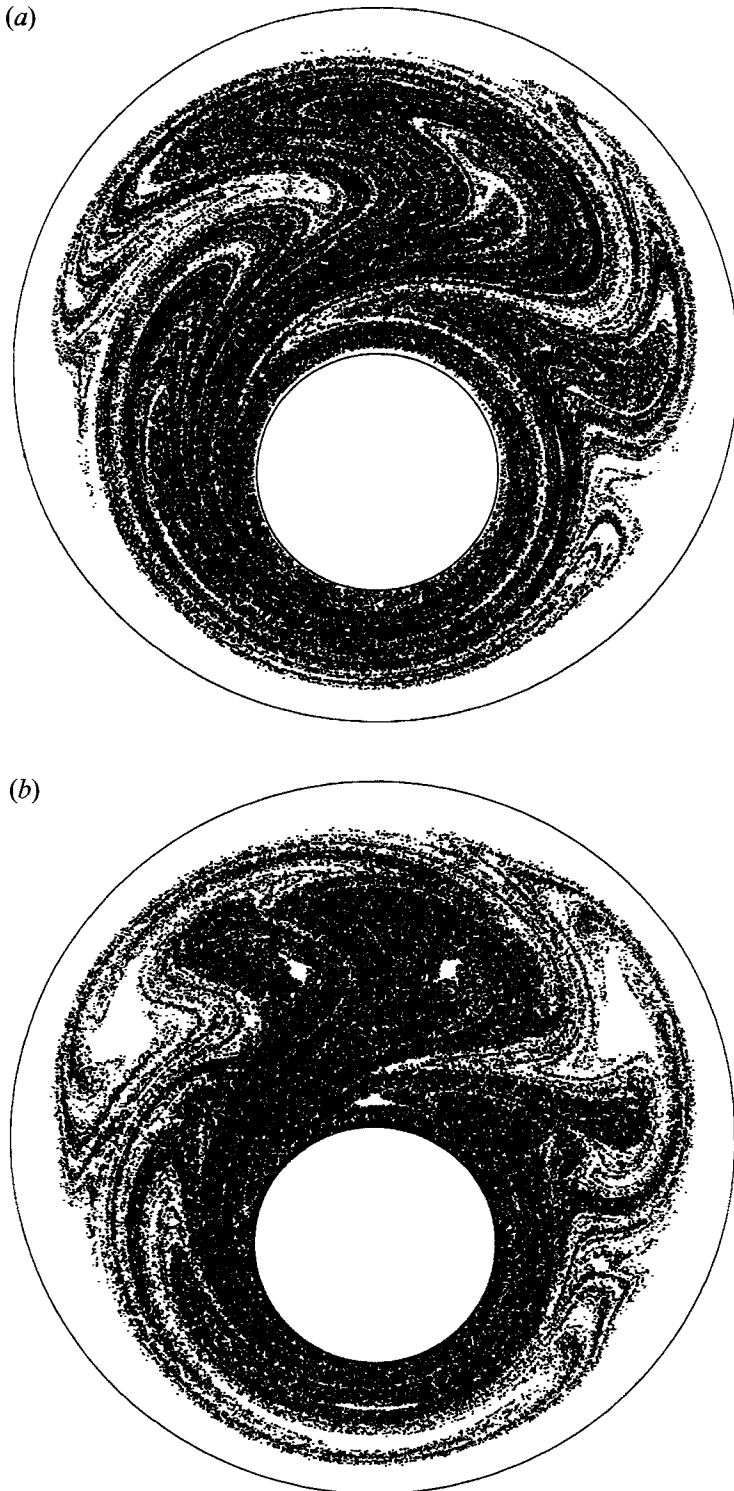


FIGURE 14. Computations of the deformation of a dye blob for $\Omega > 0$ and $\theta = \frac{3}{2}\pi$. (a) Newtonian, $N = 16$ periods; (b) $We = 0.04$, $N = 48$ periods.

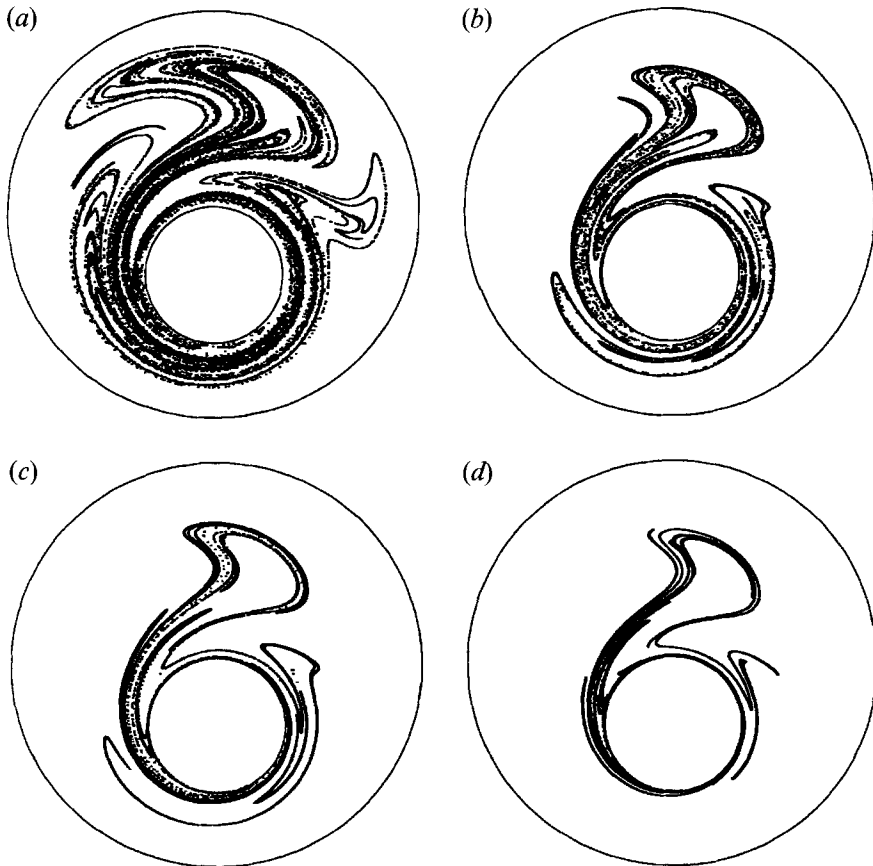


FIGURE 16. Computations of the advection of a dye blob for $\Omega > 0$ and $\theta = \frac{3}{2}\pi$. (a) Newtonian; (b) $We = 0.02$; (c) $We = 0.04$; (d) $We = 0.10$; (a–d) $N = 5$ periods.

representing the tracer and whether the points form a coherent structure. However, the effect on the rate of reduction of the average striation thickness is better demonstrated by the timescale of the mean of the separation distance.

The separation distance between adjacent points in the flow provides a quantitative measure of the effect of elasticity on the stretching of fluid elements. In order to compare computations for different θ -values, the number of periods is presented as the cumulative rotation of the outer cylinder. The correlation between the separation distance and the lineal stretching decreases significantly after 4–5 revolutions of the outer cylinder as is expected due to the folding of the tracer. The logarithm of the geometric mean of the distribution of separation distances is plotted against the number of periods for counter-rotating cylinders in figure 12. The relationship remains exponential with an increasing time constant as We increases. The time constant, T_c , defined in (28) is listed in table 2 for $We = 0, 0.01, 0.01, 0.04, \text{ and } 1.0$. The values of the time constant are similar for both θ -values in the counter-rotating flow. Curiously, the time constant for $\theta = 2\pi$ and $We = 0.01$ is slightly less than the Newtonian case; this decrease may be attributed to the contribution of the population of points in the crescent-shaped island present in the Newtonian flow.

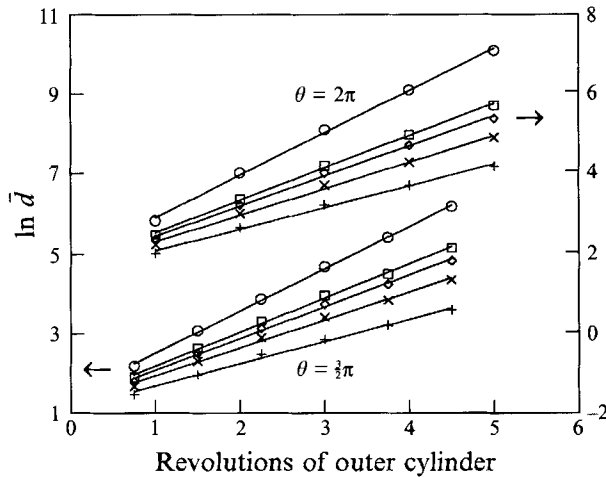


FIGURE 17. Plot of the logarithm of the geometrical mean of the distribution of the separation distance versus number of periods for $\Omega > 0$ and $\theta = \frac{3}{2}\pi$ (left axis) and $\theta = 2\pi$ (right axis): \circ , Newtonian; \square , $We = 0.01$; \diamond , $We = 0.02$; \times , $We = 0.04$; $+$, $We = 0.10$.

4.3. Corotating cylinders ($\Omega > 0$)

The unperturbed, corotating Stokes flow does not possess either hyperbolic or elliptic fixed points as illustrated by the streamlines in figure 13. Consequently, there is no period-1 elliptic point and its associated period-1 island in the perturbed Newtonian flow. Figure 14 illustrates the simulation of the advection of a tracer for $\theta = \frac{3}{2}\pi$ for a Newtonian and elastic fluid ($We = 0.04$). The Newtonian fluid contains no large low-period islands. The spatial extent of the chaotic region for the elastic fluid is comparable to the Newtonian fluid except for the presence of two sets of period-3 islands. The elasticity does have a large effect on the rate at which the tracer is mixed; 48 periods are required to develop the structure in figure 14(b) versus 16 periods for the Newtonian fluid in figure 14(a). This effect on rate can be seen in the experiments. Figure 15 (plate 2) compares the Newtonian, PAA-3 ($We = 0.05 \pm 0.02$), and PAA-1 ($We = 0.11 \pm 0.03$) fluids after 3 and 5 periods and illustrates the decrease in the amount of stretching as We increases. Figure 16 shows a similar trend in the computations for $We = 0.02, 0.04$, and 0.1 after 5 periods.

The most interesting contrast to the counter-rotating case is the large difference produced by relatively small values of We . The plots in figure 17 of the mean of the separation distances and the tabulated values of the time constant in table 2 indicate, for both θ -values, that there is a significant difference for $We = 0.01$. The large impact on the rate of stretching in the corotating flows is observed in the experiments in figure 15. Also, in contrast to the counter-rotating case, $\theta = \frac{3}{2}\pi$ appears to be more efficient at stretching fluid elements than $\theta = 2\pi$: the time constant for $\theta = \frac{3}{2}\pi$ is about 0.1 less than $\theta = 2\pi$ for all We . Note that there is essentially no difference in the time constant between the two θ -values for the Newtonian fluid.

The dependence of a normalized time constant ($T_R = T_c/T_{c,Newtonian}$) on We is shown in figure 18. For $\Omega < 0$, T_R scales with $We^{1.6}$, and for $\Omega > 0$, T_R scales with $We^{0.55}$, with a large difference even for small We . The plot also shows the sensitivity of T_R to θ for $\Omega > 0$. The rate of stretching in corotating flows is more sensitive to small changes in the kinematics; this sensitivity to Ω is intriguing in the light of the fact that the cylinders are operated in a discontinuous manner.

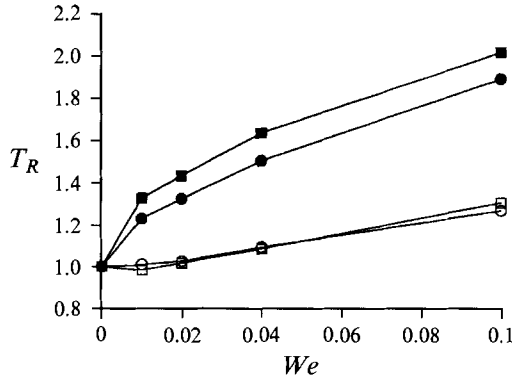


FIGURE 18. Dependence of the normalized time constant on We : \circ , \bullet , $\theta = \frac{3}{2}\pi$; \square , \blacksquare , $\theta = 2\pi$; open symbols, $\Omega < 0$; filled symbols, $\Omega > 0$. $T_R = T_c/(T_{c, Newtonian})$.

4.4. Agreement between the Maxwell model and the experimental results for a Boger fluid

The upper-convected Maxwell model is the simplest model capable of describing a fluid with memory. It has some drawbacks however. For example, it is well known that the Maxwell equation does not include the contribution to the stress from the solvent, and rheological flows of dilute polymer solutions of constant viscosity are better described by the Oldroyd-B rheological model (Binnington & Boger 1985). Because the solvent contribution to the stress satisfies the Newtonian constitutive equation, the Oldroyd-B model is not purely hyperbolic, and more computational resources and specialized algorithms are necessary to simulate the flow. However, a brief analysis of the limiting behaviour of each equation in slow flows suggests that the simpler Maxwell model is sufficient to produce the qualitative results presented in this paper.

In the limit of $De \approx 0$ and $We > 1$, all constitutive equations asymptotically approach the retarded motion expansion of the extra-stress tensor (Bird *et al.* 1987):

$$\mathbf{S} = b_1 \mathbf{G}_{(1)} + b_2 \mathbf{G}_{(2)} + b_{11}(\mathbf{G}_{(1)} \cdot \mathbf{G}_{(1)}) + b_3 \mathbf{G}_{(3)} + b_{12}(\mathbf{G}_{(1)} \cdot \mathbf{G}_{(2)} + \mathbf{G}_{(2)} \cdot \mathbf{G}_{(1)}) + b_{1;11}(\mathbf{G}_{(1)} : \mathbf{G}_{(1)}) \mathbf{G}_{(1)}, \quad (30)$$

where only the terms up to third order have been included. Since creeping flow of a second-order fluid in a plane also satisfies the biharmonic equation for the stream function (only the value of the extra-stress is affected, see Tanner 1966), it is necessary to include third-order terms to be able to describe any kinematical differences from the Newtonian case. The $\mathbf{G}_{(i)}$ are defined as

$$\mathbf{G}_{(1)} = \nabla \mathbf{v} + (\nabla \mathbf{v})^T \quad (31)$$

and
$$\mathbf{G}_{(i+1)} = \frac{D\mathbf{G}_{(i)}}{Dt} - (\nabla \mathbf{v})^T \cdot \mathbf{G}_{(i)} - \mathbf{G}_{(i)} \cdot \nabla \mathbf{v}. \quad (32)$$

The coefficients b_1, b_2, b_{11} , etc. are material constants and can be expressed as a function of the material parameters in either constitutive equation. The constants for both the Maxwell and Oldroyd-B models as a function of the material functions $\Psi_{1,0}$ and η are summarized in table 3. The retardation time λ_2 is

$$\lambda_2 = \frac{\eta_s}{\eta} \lambda_1, \quad (33)$$

	Maxwell	Oldroyd-B
b_1	η	η
b_2	$\frac{1}{2}\Psi_{1,0}$	$\frac{1}{2}\Psi_{1,0}$
b_{11}	0	0
b_3	$\frac{\Psi_{1,0}^2}{4\eta}$	$\frac{\Psi_{1,0}^2}{4\eta} + \lambda_2 \frac{\Psi_{1,0}}{2}$
b_{12}	0	0
$b_{1:11}$	0	0

TABLE 3. Representations of the Maxwell and Oldroyd-B constitutive equations in the retarded motion expansion

where η_s is the solvent contribution to the total viscosity. The Maxwell model has a zero retardation time since it does not account for the solvent contribution to the stress. However, by comparing the constants in table 3, the qualitative behaviour of both models in the slow flow limit is identical. The only difference between the two models is the magnitude of the b_3 constant. It is our opinion, that when the kinematics in a two-dimensional flow field first begin to deviate from the Newtonian flow, the deviation is qualitatively similar for both of these constitutive models. This similar behaviour in slow flows is the reason why the Maxwell model can produce the same qualitative behaviour seen in the experiments.

5. Conclusions

Small variations in the velocity field associated with mild elasticity ($We \leq 0.1$) produce large effects in the advection of a passive tracer. In fact, one of the most remarkable characteristics of chaotic systems is that a slight change in the kinematics can significantly alter the character of the periodic points and produce and/or inhibit bifurcations. This seems to be the case in this study. Both the asymptotic coverage of the dye tracer and the rate of stretching of fluid elements in the flow are affected; counter-rotating and corotating flows produce substantially different responses. The effect on the asymptotic coverage is greater for the counter-rotating case; the coverage is seen to decrease in some cases and, somewhat unexpectedly, increases in others (for example, $\theta = 2\pi$). The rate of stretching of fluid elements, as quantified by the geometrical mean of the separation distances, remains exponential for all We , with an increasing time constant as We increases for both cases of relative cylinder rotation. For corotating cylinders, the relative impact on the asymptotic coverage and rate of stretching is reversed. The asymptotic coverage is largely unaffected by $We > 0$; however, the time constant for the exponential stretching is noticeably affected even for We as small as 0.01. In all cases studied, the placement of regular regions (islands) remains symmetric since the steady-state velocity fields remain symmetric.

The difference in the results between counter-rotating and corotating cylinders is interesting since the time-periodic flow is operated in a discontinuous fashion. Since only one cylinder is rotating at any given time and both inertial and transient effects are demonstrably small, the deformation history of the fluid within a period is identical for either counter-rotating or corotating cylinders. Consequently, the differences observed between these two modes of operation must be attributed to the way the two different mappings are composed to produce the time-periodic flow.

Within a given mode of operation, the effect of elasticity on the streamline portraits

translates, in a magnified way, in different unstable manifold structures which in turn provide the template for the dye-structure pattern formed by the advection of a tracer. A physical understanding of the processes described here necessitates the development of a model describing how the presence of a polymer affects the manifold structure associated with hyperbolic points. We are aware of only one study along these lines (Berry & MacKley 1977) and more work seems possible in this regard.

The computational study indicates that the investigation of chaotic advection of viscoelastic fluids using a solution based on a discretized field is possible with an acceptable amount of error; however, techniques based on a low number of periods are better suited than those requiring asymptotic analysis (e.g. Poincaré sections). It is noteworthy that small We leads to such noticeable effects; it is also reassuring, however, that such effects can be faithfully captured with a simple constitutive equation. A few key assumptions are required to make the problem tractable. For conserving CPU time, the piecewise-steady approximation is most important. The majority of computer resources are used for the computation of the velocity field, and typical CPU times range from 3–14 days on a Digital DECstation 5000 workstation to 1–5 days on an IBM RS/6000 workstation. Because the time integration is explicit, the code can be easily adapted for parallel processors, and CPU times on a massively parallel machine could be reduced by a factor equal to the number of nodes times the number of unknowns (30000). Although the SCM-star algorithm is only appropriate for a constitutive equation with zero retardation time, other algorithms based on the Oldroyd-B equation have been developed (Keunings 1989) for steady flows and will be needed to expand the study of these fluids to cases where $We > 0.1$ within the piecewise-steady approximation. The SCM-star and other algorithms can easily incorporate nonlinear terms in the stress such as those in the Giesekus (1982) and Phan-Thien–Tanner (1977) equations, and these extensions are not difficult to implement. The main stumbling block in expanding these studies is the CPU time needed to perform a full unsteady simulation taking into account the effect of the transient fields. Because of the timescales present in the processing of polymers, the transient behaviour of these fluids might be an important consideration. Given the increase in efficiency in both algorithm development and computer architecture, the ability to assess these types of problems seems to be on the horizon. Additionally experimental studies such as the one presented in this paper coupled with analysis based on concepts from chaos and mixing theory will be needed to model the complicated behaviour in these systems. With the development and application of dynamical systems tools, more insight can be gained into the effects of elasticity, which will lead to the development of design and operating heuristics for the mixing processes of complex fluids.

The authors express their gratitude to Dr R. G. Larson (AT & T Bell Laboratories) for the rheological characterization of the experimental fluids, to Professor M. F. Malone (University of Massachusetts) and Dr F. R. Phelan (NIST) for initial assistance in improving the simulation algorithm, and to Dr M. Tjahjadi (General Electric) for assistance in the design of the experimental equipment. The authors take pleasure in acknowledging the financial support of the US Department of Energy, Office of Basic Energy Sciences.

Appendix

The split-coefficient matrix (SCM) method utilizes information propagation along characteristics while allowing one to carry out the simulation on a predetermined finite-difference grid. The following analysis is presented for a one-dimensional spatial system without loss of generality to systems with more dimensions. For a more complete discussion, the reader is referred to Anderson *et al.* (1984).

Consider an unsteady, quasi-linear partial differential system of equations:

$$w_t + \mathbf{A} \cdot w_x = f, \quad (\text{A } 1)$$

where w is a vector of unknowns of length m , \mathbf{A} is a $m \times m$ coefficient matrix whose elements can contain elements of w but not their derivatives, and f is a vector of length m of lower-order terms. The subscripts denote partial differentiation. If the system is hyperbolic, all of the eigenvalues of \mathbf{A} are real, and there are m linearly independent eigenvectors of \mathbf{A} . A diagonal matrix \mathbf{L} whose entries are the eigenvalues of \mathbf{A} is similar to the matrix \mathbf{A} ; that is

$$\mathbf{A} = \mathbf{X} \cdot \mathbf{L} \cdot \mathbf{X}^{-1} \quad (\text{A } 2)$$

where the rows of \mathbf{X}^{-1} are the eigenvectors of \mathbf{A} . In the SCM method, the coefficient matrix \mathbf{A} is split into positive and negative parts depending on the sign of the eigenvalues of \mathbf{A} . This splitting is achieved by performing a similarity transformation as in (A 2) but with only the positive or negative eigenvalues in \mathbf{L} . Thus, the split matrices \mathbf{A}^+ and \mathbf{A}^- are defined as

$$\mathbf{A}^+ = \mathbf{X} \cdot \mathbf{L}^+ \cdot \mathbf{X}^{-1} \quad (\text{A } 3)$$

and

$$\mathbf{A}^- = \mathbf{X} \cdot \mathbf{L}^- \cdot \mathbf{X}^{-1}, \quad (\text{A } 4)$$

where the diagonals of \mathbf{L}^+ and \mathbf{L}^- contain only the positive or negative eigenvalues of \mathbf{A} , and the rest of the entries are zero. The following identity holds:

$$\mathbf{A} = \mathbf{A}^+ + \mathbf{A}^-. \quad (\text{A } 5)$$

Since \mathbf{A}^+ contains the information from the positive running characteristics, and likewise for \mathbf{A}^- and the negative running characteristics, the following finite-difference approximation of (A 1) is obtained upon substitution of (A 5):

$$w_t + \mathbf{A}^+ \cdot w_x^\nabla + \mathbf{A}^- \cdot w_x^\Delta = f. \quad (\text{A } 6)$$

where the ∇ superscript denotes backward finite differences the the Δ superscript denotes forward finite differences. The equation can now be integrated using a suitable method such as Euler, Runge–Kutta, or Gear.

The major drawback to this method is that the coefficient matrix must be split at *every* node during *each* step in the integration. However, we were able to improve the speed of the algorithm by defining a new coefficient matrix:

$$\mathbf{A}^* = \mathbf{X} \cdot \mathbf{L}^* \cdot \mathbf{X}^{-1}, \quad (\text{A } 7)$$

where \mathbf{L}^* is a diagonal matrix containing the absolute values of the eigenvalues of \mathbf{A} . It follows that

$$\mathbf{A}^\pm = \frac{1}{2}(\mathbf{A} \pm \mathbf{A}^*). \quad (\text{A } 8)$$

If the split matrices in (A 6) are replaced with the expressions in (A 8), the approximating system of equations is

$$w_t + \frac{1}{2}(\mathbf{A} \cdot (w_x^\nabla + w_x^\Delta) + \mathbf{A}^* \cdot (w_x^\nabla - w_x^\Delta)) = f. \quad (\text{A } 9)$$

In this new version, SCM-star, there are analytical expressions for both coefficient matrices \mathbf{A} and \mathbf{A}^* , and the characteristics are properly treated without performing the logical conditional tests that would be necessary to split the matrix \mathbf{A} . Since the algorithm improvement exchanges logical conditional tests for floating point operations, the relative improvement is dependent on the processor architecture. For computations on a Digital VAX 11/780 the decrease in CPU time is about 50%. For computations on Unix workstations with a RISC processor, the decrease in CPU time is about 10%.

REFERENCES

- ANDERSON, D. A., TANNEHILL, J. C. & PLETCHER, R. H. 1984 *Computational Fluid Mechanics and Heat Transfer*. McGraw-Hill.
- AREF, H. 1984 Stirring by chaotic advection. *J. Fluid Mech.* **143**, 1–21.
- ASTARITA, G. & MARUCCI, G. 1974 *Principles of Non-Newtonian Fluid Mechanics*. McGraw-Hill.
- BALLAL, B. Y. & RIVLIN, R. S. 1976 Flow of a Newtonian fluid between eccentric rotating cylinders: inertial effects. *Arch. Rat. Mech. Anal.* **62**, 237–294.
- BERIS, A. N., ARMSTRONG, R. C. & BROWN, R. A. 1983 Perturbation theory for viscoelastic fluids between eccentric rotating cylinders. *J. Non-Newtonian Fluid Mech.* **13**, 109–148.
- BERIS, A. N., ARMSTRONG, R. C. & BROWN, R. A. 1987 Spectral/finite-element calculations of the flow of a Maxwell fluid between eccentric rotating cylinders. *J. Non-Newtonian Fluid Mech.* **22**, 129–167.
- BERRY, M. V. & MACKLEY, M. R. 1977 The six roll mill: unfolding an unstable persistently extensional flow. *Phil. Trans. R. Soc. Lond. A* **287**, 1–16.
- BINNINGTON, R. J. & BOGER, D. V. 1985 Constant viscosity elastic liquids. *J. Rheol.* **29**, 887–904.
- BIRD, R. B., ARMSTRONG, R. C. & HASSAGER, O. 1987 *Fluid Mechanics: Vol. 1, Dynamics of Polymeric Liquids*. 2nd edn. John Wiley & Sons.
- BOGER, D. V. 1977 A highly elastic constant viscosity fluid. *J. Non-Newtonian Fluid Mech.* **3**, 87–91.
- BURDETTE, S. R., COATES, P. J., ARMSTRONG, R. C. & BROWN, R. A. 1989 Calculations of viscoelastic flow through an axisymmetric corrugated tube using the explicitly elliptic momentum equation formulation (EEME). *J. Non-Newtonian Fluid Mech.* **33**, 1–23.
- CHAIKEN, J., CHEVRAY, R., TABOR, M. & TAN, Q. M. 1986 Experimental study of Lagrangian turbulence in a Stokes flow. *Proc. R. Soc. Lond. A* **408**, 165–174.
- CHIEN, W.-L., RISING, H. & OTTINO, J. M. 1986 Laminar mixing and chaotic mixing in several cavity flows. *J. Fluid Mech.* **170**, 355–377.
- CROCHET, M. J., DAVIES, A. R. & WALTERS, K. 1984 *Numerical Simulation of Non-Newtonian Flow*. Elsevier.
- DEBBAUT, B., MARCHAL, J. M. & CROCHET, M. J. 1988 Numerical simulation of highly viscoelastic flows through an abrupt contraction. *J. Non-Newtonian Fluid Mech.* **29**, 119–146.
- DUPRET, F. & MARCHAL, J. M. 1986 Sur le signe des valeurs propres du tenseur des extra-contraintes dans écoulement de fluide de Maxwell. *J. Mec. Theor. Appl.* **5**, 403–427.
- ELEMANS, P. H. M. 1989 Modeling of the processing of incompatible polymer blends. PhD dissertation, Eindhoven University of Technology.
- FRANJIONE, J. G. & OTTINO, J. M. 1987 Feasibility of numerical tracking of material lines and surfaces in chaotic flows. *Phys. Fluids* **30**, 3641–3643.
- GIESEKUS, H. 1982 A simple constitutive equation for polymer fluids based on the concept of deformation-dependent tensorial mobility. *J. Non-Newtonian Fluid Mech.* **11**, 69–109.
- JOSEPH, D. D. 1990 *Fluid Dynamics of Viscoelastic Liquids*. Springer.
- JOSEPH, D. D., RENARDY, M. & SAUT, J. C. 1985 Hyperbolicity and change of type in the flow of viscoelastic fluid. *Arch. Rat. Mech. Anal.* **87**, 213–251.
- KEUNINGS, R. 1989 Simulation of viscoelastic fluid flow. In *Fundamentals of Computer Modeling for Polymer Processing* (ed. Tucker, C. L.), pp. 403–469. Hanser.
- LAWLER, J. V., MULLER, S. J., BROWN, R. A. & ARMSTRONG, R. C. 1986 Laser Doppler velocimetry measurements of velocity fields and transitions in viscoelastic fluids. *J. Non-Newtonian Fluid Mech.* **20**, 51–92.

- LEONG, C.-W. & OTTINO, J. M. 1989 Experiments on mixing due to chaotic advection in a cavity. *J. Fluid Mech.* **209**, 463–499.
- LEONG, C.-W. & OTTINO, J. M. 1990 Increase in regularity by polymer addition during chaotic mixing in two dimensional flows. *Phys. Rev. Lett.* **64**, 874–877.
- MIDDLEMAN, S. 1977 *Fundamentals of Polymer Processing*. McGraw-Hill.
- MUZZIO, F. J., SWANSON, P. D. & OTTINO, J. M. 1991 The statistics of stretching and stirring in chaotic flows. *Phys. Fluids A* **3**, 822–834.
- OTTINO, J. M. 1989 *The Kinematics of Mixing: Stretching, Chaos, and Transport*. Cambridge University Press.
- PHAN-THIEN, N. & TANNER, R. I. 1977 A new constitutive equation derived from network theory. *J. Non-Newtonian Fluid Mech.* **2**, 353–365.
- PHELAN, F. R. 1989 A finite difference scheme for unsteady, nearly incompressible viscoelastic flow. PhD dissertation, University of Massachusetts.
- PHELAN, F. R., MALONE, M. F. & WINTER, H. H. 1989 A purely hyperbolic model for unsteady viscoelastic flow. *J. Non-Newtonian Fluid Mech.* **32**, 197–224.
- PILITSIS, S. & BERIS, A. N. 1989 Calculations of steady-state viscoelastic flow in an undulating tube. *J. Non-Newtonian Fluid Mech.* **31**, 231–287.
- RAUWENDAAL, C. 1991 *Mixing in Polymer Processing*. Marcel Dekker.
- RUTKEVICH, I. M. 1969 Some general properties of the equations of viscoelastic incompressible fluid dynamics. *J. Appl. Math. Mech. (Prikl. Mat. Mech.)* **33**, 42–51.
- SWANSON, P. D. 1991 Regular and chaotic mixing of viscous fluids in eccentric rotating cylinders. PhD dissertation, University of Massachusetts.
- SWANSON, P. D. & OTTINO, J. M. 1990 A comparative computational and experimental study of chaotic mixing of viscous fluids. *J. Fluid Mech.* **213**, 227–249.
- TADMOR, Z. & GOGOS, C. G. 1979 *Principles of Polymer Processing*. John Wiley & Sons.
- TANNER, R. I. 1966 Plane creeping flows of incompressible second-order fluids. *Phys. Fluids* **9**, 1246–1247.
- TJAHJADI, M. & OTTINO, J. M. 1991 Stretching and breakup of droplets in chaotic flows. *J. Fluid Mech.* **232**, 191–219.